



Design and Fabrication of a Novel On-Chip Pressure Sensor for Microchannels

| | |
|-------------------------------|---|
| Journal: | <i>Lab on a Chip</i> |
| Manuscript ID | LC-ART-07-2022-000648.R1 |
| Article Type: | Paper |
| Date Submitted by the Author: | 29-Aug-2022 |
| Complete List of Authors: | Raventhiran, Nishagar ; Montana State University, Mechanical & Industrial Engineering Molla, Razin; Montana State University, Mechanical & Industrial Engineering Nandishwara, Kshithij; Montana State University, Mechanical & Industrial Engineering Johnson, Erick; Montana State University, Mechanical & Industrial Engineering Li, Yaofa; Montana State University, Mechanical & Industrial Engineering |
| | |

Lab on a Chip

FULL PAPER

Cite this: DOI: 00.0000/xxxxxxxxxx

Design and Fabrication of a Novel On-Chip Pressure Sensor for Microchannels.[†]

Nishagar Raventhiran, Razin Sazzad Molla, Kshithij Nandishwara, Erick Johnson and Yaofa Li*

Received Date

Accepted Date

DOI: 00.0000/xxxxxxxxxx

Pressure is important in virtually all problems in fluid dynamics from macro-scale to micro/nano-scale flows. Although technologies are well developed for its measurement at the macroscopic scale, pressure quantification at the microscopic scale is still not trivial. This study reports the design and fabrication of an on-chip sensor that enables quantification of pressure in microfluidic devices based on a novel technique called astigmatic particle tracking. With this technique, thin membranes that sense pressure variations in the fluid flow can be characterized conveniently by imaging the shapes of the particles embedded in the membranes. This innovative design only relies on the reflected light from the back of the microchannel, rendering the sensor to be separate and noninvasive to the flow of interest. This sensor was then applied to characterize the pressure drop in single-phase flows with an accuracy of ~ 70 Pa and good agreement was obtained between the sensor, a commercial pressure transducer and numerical simulation results. Additionally, the sensor successfully measured the capillary pressure across an air-water interface with a 7% deviation from the theoretical value. To the best of our knowledge, this pore-scale capillary pressure quantification is achieved for the first time using an on-chip pressure sensor of this kind. This study provides a novel method for in-situ quantification of local pressure and thus opens the door to a renewed understanding of pore-scale physics of local pressure in multi-phase flow in porous media.

1 Introduction

Pressure measurement is of crucial importance in fluid mechanics to describe and understand various flows. In particular, precise measurement and control of pressure with high spatial and temporal resolutions in microfluidic systems are key to numerous scientific and engineering applications, ranging from sample manipulation in biological studies¹⁻⁴ to the evaluation of capillary pressure in multi-phase flow in porous media, which is relevant to applications like tissue engineering, biological flows, CO₂ sequestration and even enhanced oil recovery (EOR).⁵⁻⁷ For instance, capillary pressure is central to the description of multi-phase flow in porous media⁸⁻¹⁵. Conventional mathematical models of multi-phase flow in porous media have been inevitably relying on empirical relations of capillary pressure which are well known to be hysteretic^{8,9}. It is increasingly accepted that direct *in-situ* measurement of capillary pressure at the microscopic scale will be

extremely valuable to mitigate such hysteresis and thus achieve a unique description of the state of the porous medium flow system.¹⁶⁻¹⁸ As another example, in evaporative cooling¹⁹⁻²¹ and flow boiling heat transfer²², local vapor pressure in a bubble plays an important role in bubble growth and departure dynamics, which defines the overall heat transfer performance, thus rendering pressure characterization at the microscopic level a critical need to achieve a fundamental understanding of flow evaporating and boiling processes.

Currently, a number of miniature pressure sensors are commercially available with the advancement of technologies including piezoresistive, capacitive, optical, interferometric and optofluidic pressure sensors.^{23,24} However, direct integration of such sensors into microfluidic devices can be challenging because of their still relatively large sizes compared with typical microchannels. Additionally, multi-step fabrication processes are often required to enable such integration.¹⁸ Therefore, direct on-chip pressure sensors become highly promising and desirable.

In the past two decades, several on-chip pressure measurement methods have been developed employing various working principles. Abkarian et al.²⁵ were among the first ones to contribute to this advances, and they designed a differential manometer

Mechanical & Industrial Engineering Department, Montana State University, Bozeman, Montana, USA. Fax: 406-994-6292; Tel: 406-994-6773; E-mail: yaofa.li@montana.edu

* Corresponding author.

[†] Electronic Supplementary Information (ESI) available: [details of any supplementary information available should be included here]. See DOI: 00.0000/00000000.

39 based on the interface movements between two immiscible fluids in a microchannel. Alternatively, Shen et al.²⁶, Srivastava and
 40 Burns²⁷, and Hoera et al.²⁸ took advantage of the compressibility of air to measure pressure in the target channel by monitoring
 41 the volumetric response of an air bubble that was intentionally trapped in a side cavity. Probably the most popular design is the
 42 membrane-based approach. The basic idea of this design is to create a thin membrane adjacent to the target microchannel as
 43 the sensing element that deflects subject to pressure variation in the target microchannel. The membrane deflection can be read
 44 out optically or electrically, which is then correlated to the actual pressure change through a calibration step. Silicon²⁹ and poly-
 45 dimethylsiloxane (PDMS)^{17,23,30,31} are among the most common materials for building such membranes for their low cost and ease
 46 of fabrication.

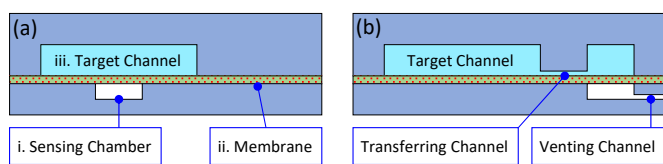


Fig. 1 Schematic diagrams illustrating the basic elements in a typical membrane-based pressure sensor: (a) a design with a closed sensing chamber directly below the target channel, and (b) a design with an open sensing chamber placed remotely to the side of the target channel.

54 A typical membrane-based pressure sensor consists of three layers as illustrated in Figure 1a: (i) a bottom layer embedded with
 55 pressure taps called sensing chambers of hundreds of micrometers thick; (ii) a sensing PDMS membrane with a thickness ranging
 56 from a few to several tens of micrometers; (iii) and a top layer containing the target channel whose thickness can range from a
 57 few micrometers to a few millimeters depending on its intended function. The three layers are often fabricated separately and
 58 then assembled employing plasma assisted bonding. While certain designs put the sensing chambers directly above or below the
 59 target flow channel³⁰ (c.f. Figure 1a), others connect the sensing chambers and the target channel *via* auxiliary transferring
 60 channels to make room for signal readout as illustrated in Figure 1b.³¹ The sensing chambers can be either closed or open to the
 61 atmosphere through a venting channel, with the latter resulting in a constant pressure within the sensing chambers, which has been
 62 shown to increase the measurement sensitivity (c.f. Figure 1b).³⁰

71 With the three-layer design, pressure measurement is conveniently transformed into quantification of membrane deflection,
 72 which has been achieved *via* approaches mainly falling into two categories: the optical schemes and the electrical schemes. The
 73 optical schemes often use a microscope and a camera to correlate the membrane deflection with a certain optical output, such as
 74 image intensity³², contrast²³ or interference patterns³⁰. Orth et al.¹⁷ characterized membrane deflection based on the goodness
 75 of focus of a reference target. When coupled with transmitted light, the membrane effectively works as a lens, which changes
 76 the optical path as deflection is increased under increasing pressure, causing the focal plane and image focus to shift accordingly.
 77 The similar idea was adopted by Chaudhury et al. in a later
 78 study²³, where membrane deflection was instead inferred based
 79 on image contrast. Song and Psaltis³⁰ leveraged interferometry,
 80 where the membrane, upon illumination by monochromatic light,
 81 generates interference patterns that depend on pressure. Chung
 82 et al.³¹ leveraged a suspension of fluorescent particles and cre-
 83 atively measured membrane deflection through the amount of
 84 depleted fluorescent particles in the sensing chamber. In general,
 85 optical schemes are accurate and easy to set up, as the required
 86 equipment (e.g., cameras and microscopes) is in many cases al-
 87 ready available in those experiments (e.g., for flow or cell visu-
 88 alization). On the other hand, the electrical schemes detect the
 89 change of electrical resistance^{33–36} or capacitance^{37,38} to infer
 90 the membrane deflection. While the electrical schemes need no
 91 more than a simple circuit and a multimeter to perform the mea-
 92 surement, the fabrication of the devices can be much more com-
 93 plicated due to the requirements of on-chip electrodes and other
 94 electrical elements. It is worth noting that recently the use of
 95 liquid metals has made such fabrication significantly easier for in-
 96 dividual pressure sensors as illustrated by Zhou et al.³⁹ and other
 97 researchers^{33,36}. However, when multiplexed microscale sensors
 98 (i.e., an array or matrix of *independent* sensors) are needed, the
 99 electrode matrix, lead wires and sensing channels can still be
 100 challenging to fabricate on polymer membranes such as PDMS.

107 Although these previous designs have greatly improved our
 108 ability to characterize pressure in various microfluidic devices, we
 109 note that none of them seems to be suited to our specific appli-
 110 cation. That is to map capillary pressure distribution in multi-
 111 phase flow in porous media^{11,15}. For instance, many previous
 112 designs used auxiliary/transferring channels to facilitate signal
 113 readout, which however adds significant dead volume to the sys-
 114 tem and thus reduces the responsiveness of the sensors.³¹ Ad-
 115 ditionally, many designs used transmitted light for signal read-
 116 out^{17,23}, where illumination light runs through all three layers:
 117 the membrane, the sensing chamber and the target channel. In
 118 that case, the output signal can be significantly affected by the
 119 flow pattern within the target channel, rendering them not suit-
 120 able for measurement of multi-phase flows. Moreover, while
 121 several studies demonstrated multiplex pressure measurement,
 122 a majority of previous designs only perform single-point mea-
 123 surements as opposed to pressure field mapping. To overcome
 124 these challenges, this work proposes a novel design of microflu-
 125 idic pressure sensor to achieve fast and precise pressure measure-
 126 ment in microchannels. In this current design, the membrane de-
 127 flection will be detected through particle astigmatism inspired by
 128 the astigmatic particle tracking velocimetry (APT_V)^{40,41}, which
 129 offers the benefits of simpler fabrication, easier implementation
 130 and better versatility. The innovation of current work is two-fold:
 131 (i) we have successfully demonstrated the effectiveness of APT_V
 132 in the quantification of membrane deflection and pressure mea-
 133 surement; (ii) we have, to the best of our knowledge, for the first
 134 time applied such pressure sensors to capillary pressure quantifi-
 135 cation in multiphase flow. This work thus paves the way for 2D
 136 pressure field mapping in porous medium flows.

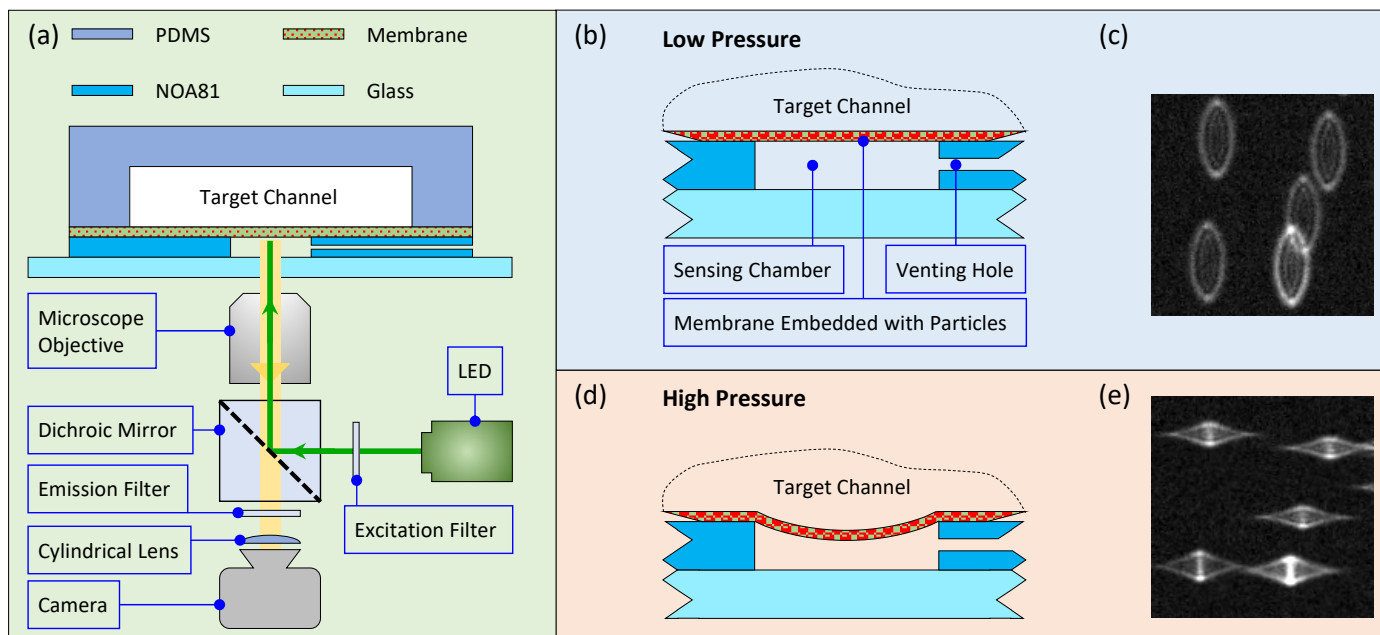


Fig. 2 (a) A schematic diagram illustrating the three-layer design of our pressure sensor: the top layer contains the flow channel made of PDMS; the middle layer is PDMS membrane with fluorescent particles embedded within; and the bottom layer contains the sensing chamber fabricated in optical glue (NOA81). Note that a glass slide is used to serve as a rigid substrate to minimize deformation of the device. (b, c) the state of the membrane and the corresponding particle images when the device is subject to *low* pressures. (d, e) the state of the membrane and the corresponding particle images when the device is subject to *high* pressures.

137 2 Experimental Description

138 2.1 Pressure Sensor Design

139 Our membrane-based pressure sensor also consists of three layers, as shown in Figure 2a. Compared with previous designs, the novel aspect of this design is that $1\ \mu\text{m}$ fluorescent particles are embedded into the sensing membrane to facilitate characterization of membrane deflection using the astigmatic particle tracking technique (see details below in § 2.2). Briefly, when the applied pressure is low, the membrane sits close to its initial position, which is far from the microscope objective (note the objective views from the bottom), causing the embedded particles to form vertical elliptical images on the camera (Figure 2b, c). As the applied pressure increases, the membrane deflects and carries the embedded particles towards the microscope objective to form horizontal elliptical images (Figure 2d, e). Essentially, the membrane deflection and thus the applied pressure are measured through the shapes of particle images. The sensing chambers placed right below the target channel are all connected to the atmosphere allowing them to stay at atmospheric pressure throughout the experiment.¹⁷ This design offers several benefits. It allows for pressure measurement at virtually any location of the target channel by conveniently positioning the sensing chamber without any modification of the setup for signal readout. By leveraging APTV, image acquisition can be performed using any standard epi-fluorescence microscope with minimal modification. Additionally, the sensor sensitivity and measurement range can be finely tuned by varying the sensing chamber size or membrane thickness. It is also worth

noting that, although this study focuses on the measurement of positive pressures in the target channel, this design is indeed ca-

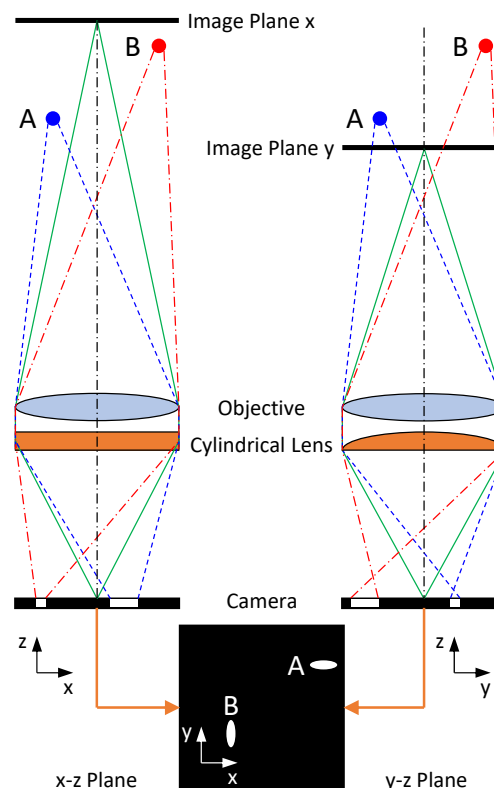


Fig. 3 A schematic illustrating the working principle of astigmatism.⁴⁰

168 pable of measuring negative gauge pressures without needing any
169 modification. Under negative pressures, the membrane would de-
170 flect upward, causing the elliptical particle images (*c.f.* Figure 2c)
171 to be even slenderer, from which and the calibration images, the
172 corresponding negative pressure can be quantified.

173 2.2 Astigmatic Particle Tracking

174 As mentioned previously, one of the innovative aspects of the de-
175 sign is the use of the APTV technique for membrane deflection
176 quantification.⁴⁰ To achieve that, (i) fluorescent tracer particles
177 are embedded in the membrane during fabrication, and (ii) a
178 cylindrical lens was placed between the microscope objective and
179 the camera as a modification to standard microscopy. As shown
180 in Figure 3, the cylindrical lens, which focuses light within a sin-
181 gle axis only, causes the imaging plane to shift in the x - z plane,
182 without affecting the y - z plane. Particles at different z locations,
183 will be focused differently in both x and y directions, forming dif-
184 ferent shapes of images depending on their z locations. Assuming
185 that there is no relative movement between the particles and the
186 membrane, particle position effectively yields information about
187 membrane deflection. In this current configuration, a particle that
188 is far away from the objective (*i.e.*, higher z location), form verti-
189 cally elongated images (particle B in Figure 3), whereas a particle
190 that is close to the objective tends to form horizontally elongated
191 images (particle A in Figure 3).

192 2.3 Fabrication

193 The device was fabricated in separate layers, which were then as-
194 sembled by bonding all layers together as shown in Figure 4. The
195 microchannel (Layer I) was fabricated employing standard soft
196 lithography⁴², which consists of three major steps: photomask
197 design, SU-8 master fabrication and PDMS molding (Figure 4,
198 Layer I). The photomask was designed in Adobe Illustrator[®],
199 and printed by a third-party company (CAD/Art Services, Inc.).
200 To create the master, a layer of SU-8 3050 (Kayaku Advanced
201 Materials SU-8 3050) was coated on a 4" silicon wafer by spin-
202 ning it at 1000 rpm for 30s, following which a series of pro-
203 cesses including soft baking, exposing, post exposure baking,
204 developing, cleaning, and hard baking were performed sequen-
205 tially, to achieve the designed pattern with a final nominal film
206 thickness of 100 μm . The SU-8 master was then silanized using
207 Trichlorosilane (Sigma-Aldrich 1H,1H,2H,2H-perfluorooctyl) for
208 30 min. Meanwhile, the PDMS polymers were prepared at a ra-
209 tio of 10:1 (pre-polymer:scuring agent), mixed, and degassed for
210 30 min to remove all air bubbles entrained in the polymer during
211 mixing. Finally, the polymer was poured on top the SU-8 master,
212 and baked at 65 °C for 2 hours to cure, following which the PDMS
213 slab was peeled off the SU-8 master, cut into individual devices,
214 and 2 mm holes were punched to serve as fluid delivery ports.

215 The membrane fabrication was conducted employing the spin-
216 coating technique as shown in Figure 4 (Layer II). The goal here
217 is to create a flexible PDMS membrane of approximately 5 μm in
218 thickness with 1 μm fluorescent particle embedded within. To this
219 end, the PDMS mixture prepared again at the 10:1 ratio was di-
220 luted by tert-butyl alcohol (TBA, $(\text{CH}_3)_3\text{COH}$) at a ratio of 1:3 by

weight (*i.e.*, 1 part of PDMS and 3 parts of TBA). TBA is a tertiary 221
alcohol and can be used to reduce the viscosity of the PDMS mix- 222
ture without causing swelling to the final cured product, which is 223
critical to create thin PDMS films as needed here.⁴³ Then 20 μl 224
suspension of carboxylate-modified fluorescent particles of 1 μm 225
in diameter (FluroSpheres, F8819) was added into 8 ml diluted 226
PDMS polymer and mixed with the aid of ultrasound. The final 227
mixture was then poured onto a silanized bare silicon wafer and 228
spun at 2000 rpm for 5 min. The PDMS film was then baked for 8 229
minutes at 65 °C to semi-cure. The microchannel (Layer I) fabri- 230
cated in the previous step was then bonded to the membrane by 231
slowly and steadily placing it onto the membrane. In this regard, 232
the semi-cure process of the membrane is critical as it ensures 233
the PDMS membrane to solidify but still sticky enough to create 234
good bonding between the two layers. The assembly of the mem- 235
brane and microchannels was fully cured in the oven for another 236
2 hours at 65 °C. 237

238 For the sensing chambers (Layer III), a PDMS mold containing 239
the sensing chamber design was first fabricated with the same 240
procedures used in Layer I, following which optical glue mold- 241
ing was conducted. The PDMS mold was placed on a flat surface 242
with the patterned side facing up. Two drops of optical glue (Nor- 243
land Optical Adhesive 81) were dispensed onto the PDMS sur- 244
face. Then a clean microscope slide (Fisher Scientific 75 \times 25 mm 245
144/GR) was placed on top of the optical glue and gently pressed 246
down to ensure the glue evenly spreads between the PDMS mold 247
and the microscope slide. The whole assembly was then exposed 248
under UV light (Thorlabs M385LP1) for 10 minutes. Once the 249
glue was cured, the PDMS mold was peeled off to expose the 250
sensing chambers made of optical glue. It is worth noting that, 251
the sensing chambers could have been fabricated in PDMS too as 252
in many previous studies^{17,23,31}. In fact, PDMS sensing cham- 253
bers were initially used in our device, and acceptable results were 254
achieved. However, we note that the optical glue used herein of- 255
fers much better optical properties compared with PDMS, which 256
helped to significantly improve the final particle image quality 257
and signal-to-noise ratio (SNR). In addition, sensing chambers 258
made of optical glue can be easily peeled off the PDMS part, al- 259
lowing for them to be reused in multiple devices. Finally, the top 260
two layers (Layers I and II) were aligned and bonded with the 261
third layer on an aligning stage (three way translation + rota- 262
tion), and the nanoports were attached to the inlet and outlet of 263
the microchannel to facilitate fluid delivery, which completes the 264
device fabrication. 265

266 2.4 Device Calibration

267 In order to use the device for accurate pressure measurement, 268
a relationship between the target pressure and membrane de- 269
flection needs to be pre-defined through a calibration step.^{17,31} 270
Herein the calibration procedure simply involves acquiring two 271
sets of images of the membrane: (i) one set of images at a series 272
of prescribed z positions, hereinafter referred to as the position 273
calibration; and (ii) a second set of images of the membrane at a 274
series of prescribed pressures, hereinafter referred to as the pres-
sure calibration. The position calibration essentially creates a li-

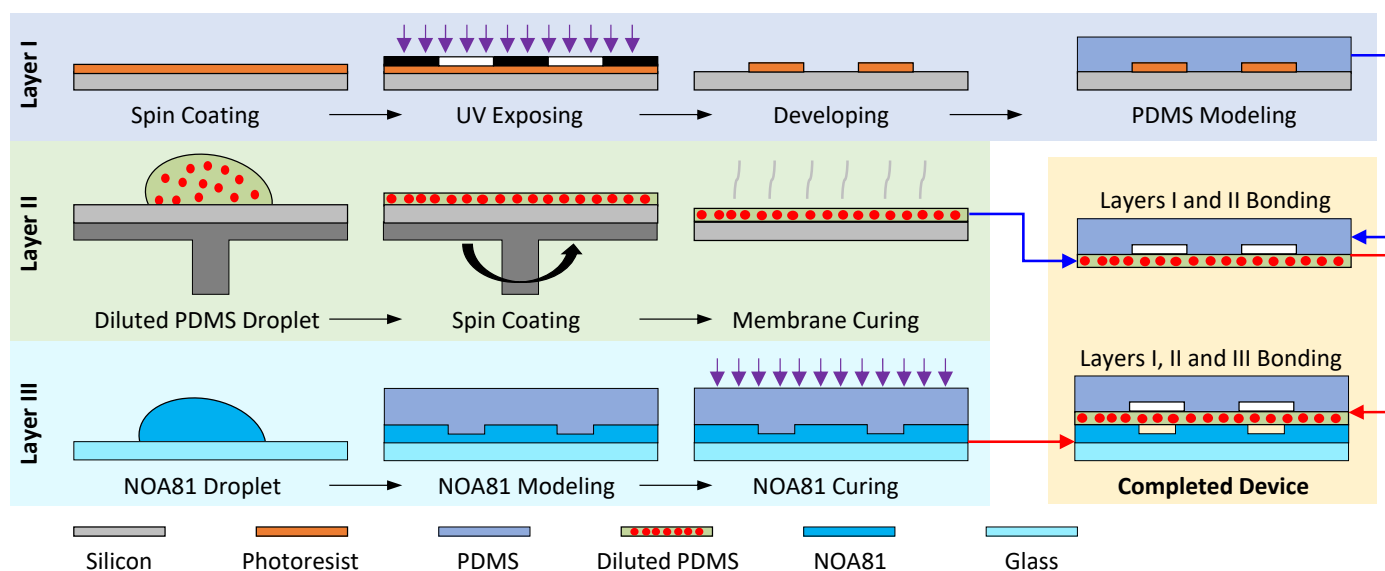


Fig. 4 Schematic illustrating the major steps to fabricate the device in layers.

275 brary of images containing information of particle image shapes
 276 at various distances from the microscope objective (Figure 5 [Left
 277 Column]). These images were used later as reference images (ef-
 278 fectively a ruler) to determine the distance between the mem-
 279 brane and the microscope objective for real experimental images.
 280 In the position calibration, the objective was initially position-
 281 ed at $z = 0 \mu\text{m}$, and gradually moved up towards the device at an in-
 282 crement of $1 \mu\text{m}$, which was precisely controlled by the focusing
 283 knob on the microscope. On the other hand, the pressure cali-
 284 bration creates a library of images at various prescribed pressures as
 285 shown in Figure 5 [Right Column]. To perform the pressure cali-
 286 bration, again the objective was initially positioned at $z = 0 \mu\text{m}$
 287 with zero pressure applied to the device. Then the applied pres-
 288 sure was gradually increased at an increment of 100 Pa , which
 289 causes the membrane to deflect downward and get closer to the
 290 objective (note again the microscope is an inverted one). The
 291 applied pressure was controlled by varying the height of an el-
 292 evated water tank which sustains hydrostatic pressure as shown
 293 in the † ESI (Figure S1). While the calibration process appears
 294 complicated, it really took no more than 15 min based on our re-
 295 peated tests. As detailed below in image analysis, by properly
 296 correlating the two sets of particle images, a relation between
 297 the applied pressure and membrane deflection can be achieved,
 298 which will be crucial to inferring pressure measurement based on
 299 particle images in real experiments.

300 2.5 Image Acquisition and Analysis

301 To facilitate device calibration and actual measurement, particle
 302 images were acquired employing the epi-fluorescence technique
 303 relying on an inverted microscope (Olympus IX-71), a scientific
 304 CMOS camera (Phantom VEO 440), and a green LED (Thorlabs
 305 SOLIS-525C M00569931). The camera sensor consist of a matrix
 306 of 2560×1600 pixels of $10 \times 10 \mu\text{m}^2$ each, resulting in a phys-
 307 ical size of $25.6 \times 16 \text{ mm}^2$, which, coupled with a $20\times$ objective
 308 and $1.2\times$ camera adaptor, produces a final field of view (FOV)

of $1.06 \times 0.67 \text{ mm}^2$. Unless otherwise noted, for each case a se- 309
 quence of 100 images were acquired at a frame rate of 25 fps. 310

The images were processed using an in-house code in MAT- 311

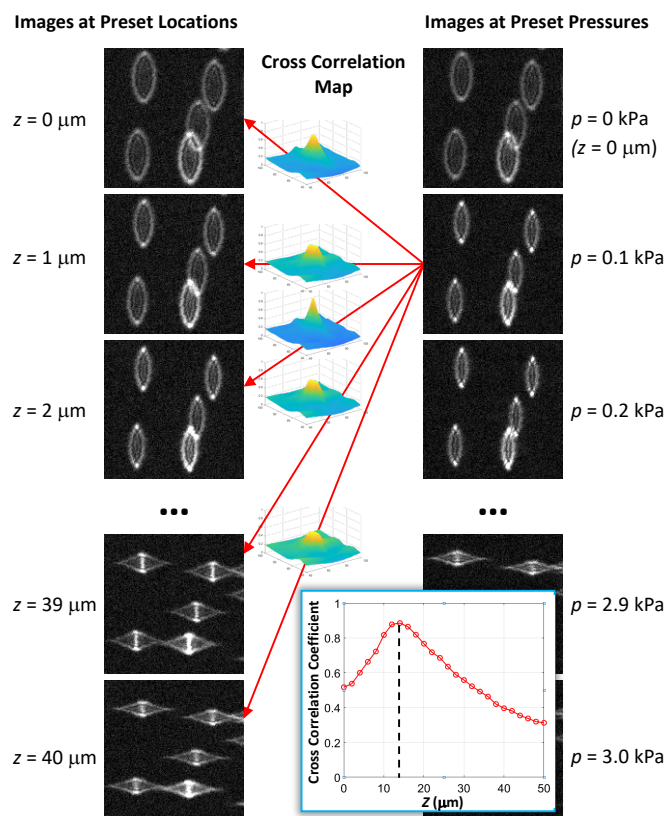


Fig. 5 A chart illustrating the calibration procedures. The left column contains the position calibration images, whereas the right column contains the pressure calibration images. Each image on the right is to be cross-correlated with all images on the left to identify the best match. The inset shows a sample fitted curve of the cross-correlation coefficients, and the uncertainty corresponding to Z position control is $0.5 \mu\text{m}$.

LAB R2019a. Briefly, a region of interest (ROI) of nominally 120×120 pixels was selected surrounding the center of the circular membrane. Extra care was used to make sure at least one fluorescent particle falls within the ROI. While a fluorescent particle does not need to be centered, the entire particle should be in view, and the size of the ROI should be adjusted accordingly. To process the calibrate images, the image acquired at each pressure (e.g., $p = 0.1$ kPa in Figure 5) was cross-correlated with all position calibration images, and cross-correlation coefficients were calculated between the specific pressure calibration image and all position calibration images. Here the goal is to identify the position calibration image that is the most similar to the specific pressure calibration image, which is evaluated based on the cross-correlation coefficient (i.e., a higher cross-correlation coefficient indicates a better similarity between two images). with all coefficients calculated, a polynomial curve was fitted using the built-in “polyfit” function in MATLAB to identify the best match based on the peak value of the curve (c.f. Figure 5 inset). Since the objective position is fixed in the pressure calibration, the z location of the identified position calibration image effectively measures the amount of deflection corresponding to the specific pressure calibration image. Using this approach, each pressure calibration image was matched with a position calibration image, essentially producing a relationship between the applied pressure and the membrane deflection (Figure 6).

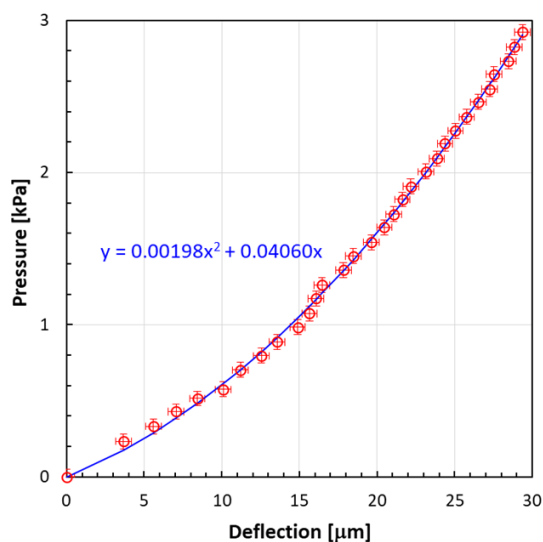


Fig. 6 Calibrated relationship between applied pressure (kPa) and membrane deflection (μm) obtained for one pressure sensor used in this study. The horizontal error bars represent the uncertainty of Z position control (i.e., $0.5 \mu\text{m}$) and the vertical error bars represent the uncertainty of hydrostatic pressure control (i.e., 0.05 kPa).

Processing of an actual measurement image taken at an unknown pressure essentially follows the same way. The target image at the unknown pressure (i.e., to be measured) again was cross-correlated with all position calibration images, and cross-correlation coefficients were calculated. The position calibration image that yields the highest coefficient was then identified, which effectively measures the amount of deflection correspond-

ing to the target image. The deflection was then substituted into the pressure-deflection relation obtained in the calibration step (i.e., Figure 6) to determine the unknown pressure, which completes the measurement.

3 Results and Discussion

3.1 Calibrated Pressure-Deflection Relation

Figure 6 shows the pressure–deflection relation obtained for one pressure sensor, which was calibrated in the range of 0 – 2.9 kPa. As expected, the applied pressure and membrane deflection show good linearity for small deflection in the pressure range of 0 – 1 kPa with a sensitivity of ~ 0.066 kPa/ μm . In the higher pressure range, non-linearity starts to arise with an average sensitivity of 0.13 kPa/ μm . To facilitate pressure calculation and interpolation, a second order polynomial was used to fit the data in the entire range of 0 – 2.9 kPa. The root mean square deviation (RMSD) between the data points and the fitted curve is less than 0.04 kPa, corresponding to $\sim 1.4\%$ of the full-scale value of 2.9 kPa. It is worth noting that in the current study, all the membranes and sensing chambers were fabricated following exactly the same procedures and recipes in a highly repeatable manner, so the calibration curves are highly similar between different devices and different sensors. While it is possible to use the same calibration curve for all sensors with acceptable accuracy, we produced a separate ad hoc calibration curve for each individual sensing chamber and membrane to ensure high accuracy. In addition, to rigorously test the pressure sensor for its robustness and potential hysteresis, a test calibration was also performed for 4 consecutive runs using a separate sensor fabricated in the same way, where the applied pressure was varied following a pattern of 0 kPa – 2.4 kPa – 0 kPa – 2.4 kPa – 0 kPa at a step of 0.2 kPa. As shown in † ESI Figure S5, the data from all 4 runs agrees very well, with a maximum RMSD of 0.042 kPa (1.75% of the calibrated range) between any two runs, suggesting a good repeatability and negligible hysteresis of the pressure sensor in the calibrated range.

3.2 Application: Pressure Drop in Single-Phase flow

As the first application and validation of the pressure sensor, the pressure drop in a microchannel was measured using both air and deionized (DI) water as the working fluids at constant flow rates. For this measurement, a microchannel of a nominal width, height and length of $w = 0.1$ mm, $h = 0.12$ mm, and $l = 18.8$ mm, respectively, were fabricated as shown in Figure 7. To the upstream and downstream of the test channel, two short channels with enlarged width ($w = 0.3$ mm) were added to connect the test channel with the inlet and outlet. The pressure sensors were then incorporated right at the upstream of the inlet and the downstream of the outlet to effectively measure the pressure drop across the entire test microchannel. It is worth noting that the test microchannel was intentionally designed to have a U shape to: (i) reduce the footprint of the device, and (ii) place the upstream and downstream sensors close by so that they can be measured simultaneously by fitting both in one FOV of the microscope. For all sensors used in this study, the sensing chambers were $200 \mu\text{m}$ in diameter, and $\sim 80 \mu\text{m}$ in depth. As illustrated in Figure 7a, the

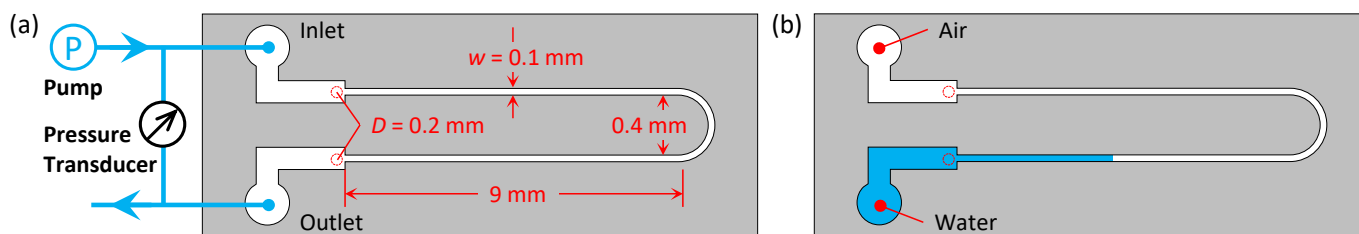


Fig. 7 Schematic illustrating the pressure drop measurement setup for the single-phase flow (a) and multi-phase flow (b) cases. The test microchannel is 0.1 mm wide, 0.12 mm depth and 18.8 mm long. And the pressure sensors used herein are all 0.2 mm in diameter. The flow rate is controlled by a syringe pump connected to the inlet of the microchannel, whereas the outlet is opened to atmosphere. In the single-phase flow case, the pressure drop across the microchannel is also measured with a differential pressure transducer. In the multi-phase flow case, air was used to displace water at a very low flow rate, and the pressure drop is dominated by the capillary pressure jump across the interface.

397 flow was controlled by a high-precision syringe pump (Harvard
 398 Apparatus, PHD 22/2000). Additionally, the pressure different
 399 between the inlet and outlet was also measured by a commercial
 400 pressure transducer (Validyne, P55E) as a benchmark reference,
 401 whose reading was continuously logged using a data acquisition
 402 system (National Instruments, USB-6001).

403 For the air flow experiment, the pressure drop was measured at
 404 flow rates from 0 to 1.2 ml/min with an increment of 0.1 ml/min.
 405 The Reynolds number at the maximum flow rate of 1.2 ml/min
 406 was calculated to be 11.6 based on the hydraulic diameter of the
 407 microchannel, confirming the laminar flow conditions. Following
 408 each increase of flow rate, a minimum waiting time of 1 min
 409 was used to ensure a steady-state flow during image acquisition. The
 410 same MATLAB image analysis algorithm as described in the cali-
 411 bration procedures was used to calculate the membrane deflection
 412 for each applied flow rate. Once the membrane deflection
 413 was determined, it was substituted into the pressure-deflection
 414 relation (*i.e.*, Figure 6) to determine the pressure exerted at each
 415 of the pressure sensors at upstream and downstream. The differ-
 416 ence between the two pressures yielded the pressure drop across
 417 the microchannel.

418 Figure 8a shows the variation of pressure drop within the mi-
 419 crochannel as a function of flow rate. As expected for laminar
 420 flows, the pressure drop is proportional to the flow rate, result-
 421 ing in a linear relationship. The error bars represent the combined er-
 422 ror propagated from uncertainties in the calibration relation and
 423 uncertainties in the membrane deflection calculation. To validate
 424 the pressure sensor measurement, it is compared with the data
 425 obtained with the commercial pressure transducer. It can be seen
 426 that the two sets of measurement agree very well yielding a RMSD
 427 of 0.028 kPa and a maximum deviation of 0.045 kPa, $\sim 1.5\%$
 428 of the full scale value. To further validate the experimental mea-
 429 surement, the pressure drop across the microchannel was also numer-
 430 ically calculated using Star-CCM+ (see † ESI for details), which
 431 was plotted in Figure 8. The numerical results agrees reasonably
 432 well with the experimental measurements with a slight overpre-
 433 diction at the high pressure range. Although this overprediction is
 434 within the measurement uncertainty, we believe this discrepancy
 435 can also be partially attributed to the slight deformation (expan-
 436 sion) of the PDMS microchannel under high pressures⁴⁴, which
 437 was not considered in the simulation. We also note that the pres-
 438 sure drop in a rectangular channel at a given flow rate can also

be theoretically calculated based on the following equation⁴⁵,

$$\Delta p = \frac{4\mu l}{wh^3 \left[\frac{1}{3} - \frac{64h}{\pi^3 w} \tanh\left(\frac{\pi w}{2h}\right) \right]} Q \quad (1)$$

440 where μ is the dynamic viscosity of the working fluid, and Q is the
 441 volumetric flow rate through the microchannel. Although data
 442 is not shown here, the theoretical values are also in reasonable
 443 agreement with the experimentally measured values. However,
 444 after careful measurement, it was observed that the microchannel
 445 used herein does not have a perfect rectangular cross-section. In-
 446 stead the cross-sectional is more of a trapezoid shape with curved
 447 edges (see † ESI Figure S2). Therefore, we believe the numerical
 448 simulation result, which was based on the actual 3D geometry of
 449 the microchannel, provides a better representation of the actual
 450 pressure drop in the microchannel as shown in Figure 8a.

451 The same experiment was performed using DI water as the
 452 working fluid at different flow rates. Due to the much higher
 453 dynamic viscosity of water compared with air, the flow rate was
 454 reduced by about two orders of magnitude, so that the pressure
 455 drop falls within the measurement range of the sensors. The
 456 Reynolds number corresponding to the highest flowrate is 1.4,
 457 again confirming laminar flows in the microchannel. Figure 8b
 458 shows the variation of pressure drop within the microchannel
 459 as a function of flow rate using DI water as the working fluid.
 460 Again a good linear relationship between pressure drop and flow
 461 rate is evident, as expected for laminar flows. All three sets of
 462 data show reasonably good agreement, with a RMSD value of
 463 0.036 kPa between the pressure sensor and pressure transducer
 464 measurements. It is also worth noting that, to quantify the poten-
 465 tial hysteresis of the pressure sensor, pressure drop was also mea-
 466 sured by reducing the flow rate from high to low at selected flow
 467 rates (*i.e.*, 1.2 ml/min back to 0 ml/min at a step of 0.2 ml/min
 468 in the air case, and 8 μ l/min back to 0 μ l/min at a step of 2 μ l/min
 469 in the water case). The maximum deviations between the up and
 470 down runs are 0.04 kPa and 0.03 kPa for the air and water cases,
 471 respectively, which both fall within the measurement uncertainty,
 472 confirming very little, if any, hysteresis of the pressure sensor.

3.3 Application: Capillary Pressure in Multi-Phase Flow

473 The capillary pressure measurement in an air-water multi-phase
 474 flow was conducted using a similar setup as used for the single-
 475

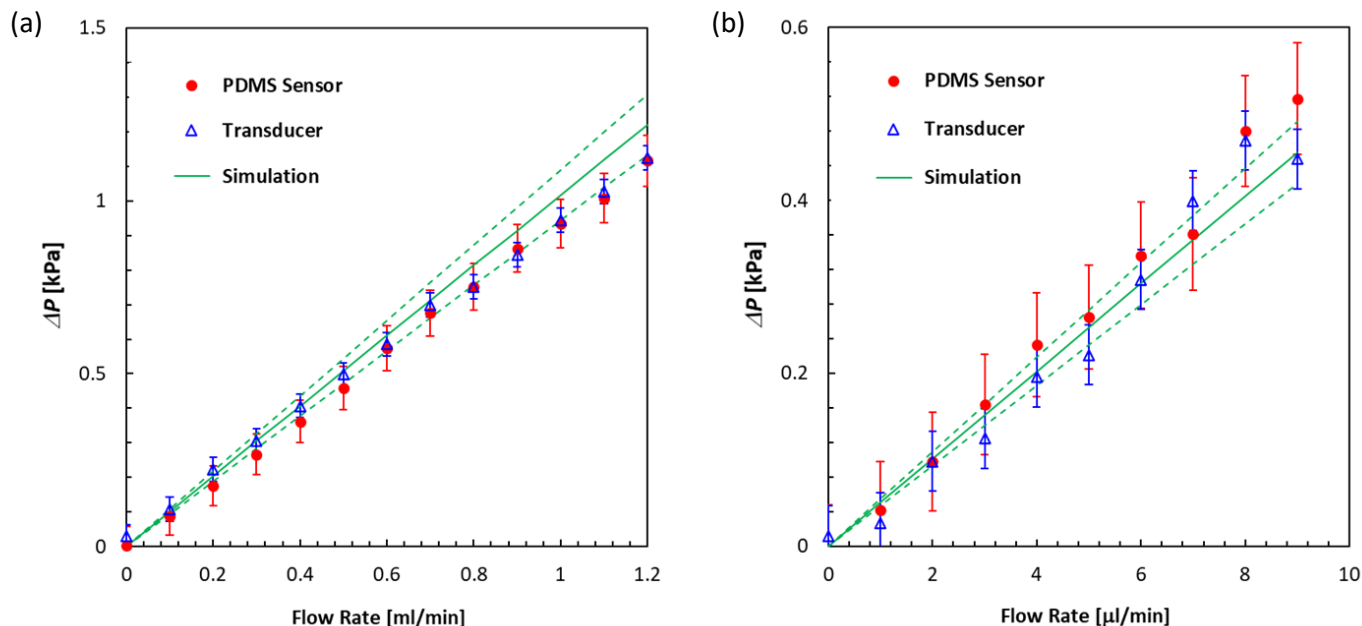


Fig. 8 Pressure drop at various flow rates obtained using our sensor (red symbols), the commercial pressure transducer (blue symbols) and numerical simulation (green lines) for the single-phase flows of air (a) and water (b). The error bars associated with the PDMS sensor data indicated the overall propagated uncertainties (0.07 kPa, $\sim 2.4\%$ of the full scale value) from the calibrate relation and membrane deflection measurement. The transducer data error bars are based on the manufacturer-specified accuracy. And the dashed lines are the upper and lower bounds of the numerical values ($\pm 8\%$), again based on propagated errors mainly from channel dimension measurements.

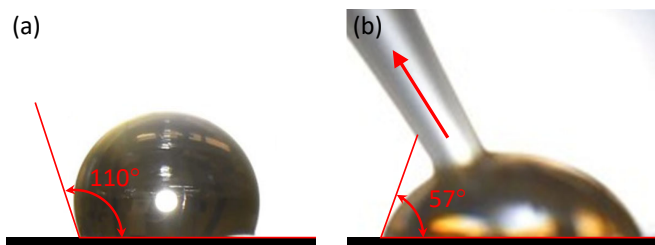


Fig. 9 Photos of water droplets on a PDMS surface under (a) static condition and (b) receding condition. To create the receding contact line, the water was instantaneously withdrawn from the droplet using a pipette. Both images were processed in ImageJ, and the static and receding contact angles turned out to be 110° and 57° , respectively.

476 phase flow. To initiate the experiments, the microchannel was
 477 first presaturated with DI water using the syringe pump at a flow
 478 rate of $5 \mu\text{l}/\text{min}$. Extra care was taken during this step to prevent
 479 any air bubbles from getting into the microchannel. Then the sy-
 480 ringe pump was paused for a minimum of 5 min to allow the flow
 481 to subside. Next air was slowly injected into the microchannel at
 482 the same flow rate of $5 \mu\text{l}/\text{min}$. As the air enters the microchan-
 483 nel, an air-water interface is created, which generates a pressure
 484 jump (capillary pressure) across the interface due to surface ten-
 485 sion and interfacial curvature. It is worth noting that PDMS is
 486 slightly hydrophobic under static conditions. In fact, our mea-
 487 surement shows that the static contact angle of water on PDMS
 488 surface is 110° (Figure 9a). However, in this case when water is
 489 being displaced out of the microchannel, what is relevant is the
 490 receding contact angle. Our measurement indicated a receding
 491 contact angle of 57° for a droplet water shrinking on PDMS sur-

face (Figure 9b). The entire process of air displacing water was
 recorded and again processed in MATLAB as discussed earlier.

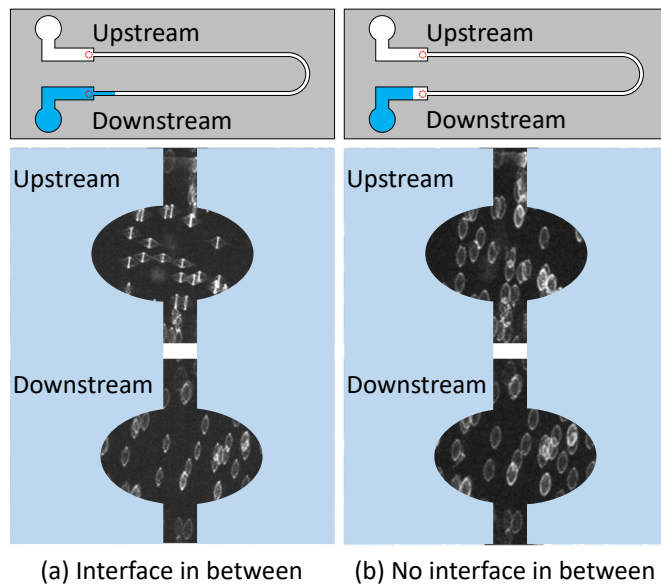


Fig. 10 Particle image shapes of the upstream and downstream sensors before (a) and after (b) the air-water interface passes the downstream sensor. When capillary pressure jump exists between the two sensors (a), the upstream sensor is subject to high pressure; when the interface exits the test channel (b), both sensors are subject to low pressure.

Figure 10 shows the raw particle images for both upstream and
 downstream sensors, right before and after the air-water inter-
 face passes the downstream sensor. When the air-water inter-

face is between the two pressure sensors (Figure 10a), the membrane in the upstream sensor undergoes a large deflection as evident from the horizontally elongated particle images, suggesting a high pressure is exerted on the upstream pressure sensor. The downstream sensor on the other hand shows very little membrane deflection as evident from the vertically elongated particle images. Due to the low dynamic viscosity of air and the extremely low flow rate, the contribution of viscous pressure drop of air is largely negligible. Therefore, the pressure difference between the upstream and downstream sensors is essentially due to the capillary pressure generated across the interface. However, when the air-water interface passes the downstream sensor (Figure 10b), the upstream sensor immediately resumes to its initial condition, with little pressure difference detected between the upstream and downstream sensors, as expected.

Based on the particle images, the capillary pressure across the air-water interface in the microchannel was measured to be 1.54 kPa. A theoretical value of the capillary pressure was calculated using the Young-Laplace equation based on the microchannel dimensions, the water-air surface tension and the receding contact angle¹⁶,

$$p^c = 2\sigma\left(\frac{1}{w} + \frac{1}{d}\right)\cos\theta \quad (2)$$

where p^c is the capillary pressure, σ is the surface tension of water (0.072 N/m), w and d are the width (0.096 mm) and depth (0.12 mm) of the microchannel, respectively, and θ (57°) is the receding contact angle of the water phase. Note due to the trapezoidal shape of the cross section, w here was taken at the narrowest point, which is believed to dominate the capillary pressure¹⁶. Based on Equation 2 and the physical values, the theoretical capillary pressure was calculated to be 1.47 kPa, which deviates from the measured value by 0.07 kPa (4.5%), within the measurement uncertainty of 0.07 kPa of the pressure sensor. This result represents a big improvement compared with previous capillary pressure measurement based on interfacial curvature¹⁶.

The last thing to note is that properties of PDMS are known to change over time (e.g., bulk materials get stiffer over time)⁴⁶. To ensure that our results are not significantly impacted by this effect, all the experiments were performed within 10 hours of the calibration. Additionally, a stability test was carried out to determine the change of the calibration curve of the same sensor over 24 hours. The membrane indeed got slightly more rigid over time, leading to a higher pressure in the second test for the same amount of membrane deflection. Although results are not shown, the RMSD between the two curves is found to be 0.035 kPa, which is ~1.2% of the full scale. Nevertheless, this relatively small shift of material properties further justifies our measurement quality.

4 Conclusions

A membrane-based microfluidic pressure sensor has been successfully designed and fabricated using simple soft lithography. By embedding 1 μ m fluorescent particles into the thin membrane, and using Astigmatic Particle Tracking scheme, the membrane deflection is detected based on the shape of the particles. The simple optical readout method and image processing algorithm

have led to fast and precise pressure measurements under single and multi-phase flow conditions in the microchannel. The current sensor has a measurement range of 0–2.9 kPa with an accuracy of 70 Pa. The sensor has been successfully applied to measure the pressure drop within a microchannel for single-phase flow of air and DI water. Good agreement has been achieved between the pressure sensor, a commercial pressure transducer and numerical simulation results. Additionally, to the best of our knowledge, the sensor has for the first time successfully measured the capillary pressure across the air-water interface with a 7% deviation from the theoretical value. The capability demonstrated by the pressure sensor is promising and this work opens the door to a renewed understanding of pore-scale physics of multi-phase flow in porous media.

Although the current study only demonstrated the use of two pressure sensors in a microchannel, as the next step a 2D array of pressure taps will be fabricated to enable a true 2D pressure field mapping, which can be achieved by a simple change of the photomask design. Moreover, although not explored in the current study, the sensitivity and measurement range of the pressure sensor can be finely tuned by adjusting parameters such as the pressure sensor size, PDMS membrane thickness, and even the Young's modulus of the PDMS material. A parametric study of the system will be carried out in a future study to gain a better understanding of the device performance, and help to accommodate more challenging measurements, such as 2D pressure mapping of multi-phase flow in porous media. Finally, surface wettability is a well-known issue of the PDMS material. Although the naturally hydrophobic PDMS surfaces can be made hydrophilic by exposing them to an air or oxygen plasma, such modification is known to be unstable⁴⁷. Additionally, PDMS itself is incompatible with many solvents and oils, all of which may limit its application in many multi-phase flow scenarios⁴⁸. To partially alleviate this issue, we will explore different elastic materials and/or different types of coatings to further expand its compatibility.

Author Contributions

Nishagar Raventhiran: Methodology, Data acquisition, Data curation, Writing - Original draft preparation. Razin Sazzad Molla: Methodology, Data acquisition. Kshithij Nandishwara: Software, Data curation, Validation. Erick Johnson: Supervision, Software, Writing- Reviewing and Editing. Yaofa Li: Conceptualization, Methodology, Data acquisition, Data curation, Writing- Reviewing and Editing.

Conflicts of interest

There are no conflicts to declare.

Acknowledgements

This work was performed in part at the Montana Nanotechnology Facility, a member of the National Nanotechnology Coordinated Infrastructure (NNCI), which is supported by the National Science Foundation (Grant ECCS-1542210). This work was partially supported by the Murdock Charitable Trust. We are grateful to the Faculty Excellence Grants and the Norm Asbjornson College of Engineering at Montana State University for their support. We

602 also thank Dr. Andrew Lingley and Dr. Joshua Heinemann at
603 Montana Microfabrication Facility for their help with the device
604 fabrication.

605 References

- 606 1 T. Matsunaga, M. Hosokawa, A. Arakaki, T. Taguchi, T. Mori,
607 T. Tanaka and H. Takeyama, *Analytical chemistry*, 2008, **80**,
608 5139–5145.
- 609 2 M. M. Crane, K. Chung, J. Stirman and H. Lu, *Lab on a Chip*,
610 2010, **10**, 1509–1517.
- 611 3 J. G. Shackman, G. M. Dahlgren, J. L. Peters and R. T.
612 Kennedy, *Lab on a Chip*, 2005, **5**, 56–63.
- 613 4 P. J. Lee, T. A. Gaige and P. J. Hung, *Lab on a Chip*, 2009, **9**,
614 164–166.
- 615 5 J. E. McClure, S. Berg and R. T. Armstrong, *Physics of Fluids*,
616 2021, **33**, 083323.
- 617 6 C. Garing, J. A. de Chalendar, M. Voltolini, J. B. Ajo-Franklin
618 and S. M. Benson, *Advances in Water Resources*, 2017, **104**,
619 223–241.
- 620 7 A. L. Herring, J. Middleton, R. Walsh, A. Kingston and
621 A. Sheppard, *Advances in Water Resources*, 2017, **107**, 460–
622 469.
- 623 8 R. T. Armstrong, J. E. McClure, M. A. Berrill, M. Rücker,
624 S. Schlüter and S. Berg, *Physical Review E*, 2016, **94**, 043113.
- 625 9 W. G. Gray, K. Bruning and C. T. Miller, *Journal of Hydraulic*
626 *Research*, 2019, **57**, 747–759.
- 627 10 H. E. Huppert and J. A. Neufeld, *Annu. Rev. Fluid Mech*, 2014,
628 **46**, 255–272.
- 629 11 Y. Li, G. Blois, F. Kazemifar and K. T. Christensen, *Water Re-*
630 *sources Research*, 2019, **55**, 3758–3779.
- 631 12 Y. Chen, Y. Li, A. J. Valocchi and K. T. Christensen, *Journal of*
632 *Contaminant Hydrology*, 2018, **212**, 14–27.
- 633 13 A. Fakhari, Y. Li, D. Bolster and K. T. Christensen, *Advances in*
634 *Water Resources*, 2018, **114**, 119–134.
- 635 14 Y. Li, F. Kazemifar, G. Blois and K. T. Christensen, *Water Re-*
636 *sources Research*, 2017, **53**, 6178–6196.
- 637 15 Y. Li, G. Blois, F. Kazemifar and K. T. Christensen, *Measure-*
638 *ment Science and Technology*, 2021.
- 639 16 N. Karadimitriou, S. Hassanizadeh, V. Joekar-Niasar and
640 P. Kleingeld, *Water Resources Research*, 2014, **50**, 8125–8140.
- 641 17 A. Orth, E. Schonbrun and K. B. Crozier, *Lab on a Chip*, 2011,
642 **11**, 3810–3815.
- 643 18 I. Zarikos, S. Hassanizadeh, L. van Oosterhout and W. van
644 Oordt, *Transport in porous media*, 2018, **122**, 221–234.
- 645 19 Y. Li, R. Grigoriev and M. Yoda, *Physics of Fluids*, 2014, **26**,
646 122112.
- 647 20 Y. Li and M. Yoda, *Experiments in Fluids*, 2014, **55**, 1–11.
- 648 21 Y. Li and M. Yoda, *International Journal of Heat and Mass*
649 *Transfer*, 2016, **102**, 369–380.
- 650 22 Y. Zhu, D. S. Antao, K.-H. Chu, S. Chen, T. J. Hendricks,
651 T. Zhang and E. N. Wang, *Journal of Heat Transfer*, 2016, **138**,
652 year.
- 653 23 A. Chaudhury, A. Pantazis and N. Chronis, *Sensors and Actua-*
654 *tors A: Physical*, 2016, **245**, 63–67.
- 24 S. H. Aref, H. Latifi, M. I. Zibaii and M. Afshari, *Optics com-*
655 *munications*, 2007, **269**, 322–330. 656
- 25 M. Abkarian, M. Faivre and H. A. Stone, *Proceedings of the*
657 *National Academy of Sciences*, 2006, **103**, 538–542. 658
- 26 F. Shen, M. Ai, J. Ma, Z. Li and S. Xue, *Micromachines*, 2020,
659 **11**, 914. 660
- 27 N. Srivastava and M. A. Burns, *Lab on a Chip*, 2007, **7**, 633–
661 637. 662
- 28 C. Hoera, A. Kiontke, M. Pahl and D. Belder, *Sensors and Ac-*
663 *tuator B: Chemical*, 2018, **255**, 2407–2415. 664
- 29 D. Wagner, J. Frankenberger and P. Deimel, *Journal of Mi-*
665 *cromechanics and Microengineering*, 1994, **4**, 35. 666
- 30 W. Song and D. Psaltis, *Optics letters*, 2010, **35**, 3604–3606. 667
- 31 K. Chung, H. Lee and H. Lu, *Lab on a Chip*, 2009, **9**, 3345–
668 3353. 669
- 32 V. A. ROSSI and M. A. CARPENTER, *Sensors & Transducers*,
670 2019, **239**, 34–40. 671
- 33 T. Jung and S. Yang, *Sensors*, 2015, **15**, 11823–11835. 672
- 34 D.-W. Lee and Y.-S. Choi, *Microelectronic Engineering*, 2008,
673 **85**, 1054–1058. 674
- 35 X. Liu, Y. Zhu, M. W. Nomani, X. Wen, T.-Y. Hsia and G. Koley,
675 *Journal of Micromechanics and Microengineering*, 2013, **23**,
676 025022. 677
- 36 C.-Y. Wu, W.-H. Liao and Y.-C. Tung, *Lab on a Chip*, 2011, **11**,
678 1740–1746. 679
- 37 C.-L. Dai, P.-W. Lu, C. Chang and C.-Y. Liu, *Sensors*, 2009, **9**,
680 10158–10170. 681
- 38 P.-J. Chen, D. C. Rodger, S. Saati, M. S. Humayun and Y.-
682 C. Tai, *Journal of Microelectromechanical Systems*, 2008, **17**,
683 1342–1351. 684
- 39 X. Zhou, R. Zhang, L. Li, L. Zhang, B. Liu, Z. Deng, L. Wang
685 and L. Gui, *Lab on a Chip*, 2019, **19**, 807–814. 686
- 40 C. Cierpka, M. Rossi, R. Segura and C. Kähler, *Measurement*
687 *Science and Technology*, 2010, **22**, 015401. 688
- 41 Y. Ichikawa, K. Yamamoto and M. Motosuke, *Microfluidics and*
689 *Nanofluidics*, 2018, **22**, 1–9. 690
- 42 Y. Xia and G. M. Whitesides, *Angewandte Chemie International*
691 *Edition*, 1998, **37**, 550–575. 692
- 43 J. H. Koschwanetz, R. H. Carlson and D. R. Meldrum, *PLoS*
693 *one*, 2009, **4**, e4572. 694
- 44 B. S. Hardy, K. Uechi, J. Zhen and H. P. Kavehpour, *Lab on a*
695 *Chip*, 2009, **9**, 935–938. 696
- 45 M. Bahrami, M. Yovanovich and J. Culham, International Con-
697 ference on Nanochannels, Microchannels, and Minichannels,
698 2005, pp. 269–280. 699
- 46 M. Kim, B.-U. Moon and C. H. Hidrovo, *Journal of Microme-*
700 *chanics and Microengineering*, 2013, **23**, 095024. 701
- 47 N. Karadimitriou, M. Musterd, P. Kleingeld, M. Kreutzer,
702 S. Hassanizadeh and V. Joekar-Niasar, *Water Resources Re-*
703 *search*, 2013, **49**, 2056–2067. 704
- 48 J. N. Lee, C. Park and G. M. Whitesides, *Analytical chemistry*,
705 2003, **75**, 6544–6554. 706